Title

Semiautomatic registration of digital histopathology images to in vivo MR images in molded and unmolded prostates

Journal

Journal of Magnetic Resonance Imaging, 39(5)

ISSN

1053-1807

Authors

Starobinets, Olga
Guo, Richard
Simko, Jeffry P
et al.

Publication Date

2014-05-01

DOI

10.1002/jmri.24287

Peer reviewed

Published in final edited form as:
J Magn Reson Imaging. 2014 May ; 39(5): 1223–1229. doi:10.1002/jmri.24287.

Semi-automatic registration of digital histopathology images to in-vivo MR images in molded and unmolded prostates

Olga Starobinets, MS[1], **Richard Guo, BS**[2], **Jeffry P. Simko, MD, PhD**[3,4], **Kyle Kuchinsky, BS**[3], **John Kurhanewicz, PhD**[1,5], **Peter R. Carroll, MD, MPH**[4], **Kirsten L. Greene, MD, MS**[4], and **Susan M. Noworolski, PhD**[1,5]

[1]Department of Radiology and Biomedical Imaging, University of California, San Francisco

[2]Medical School, University of Minnesota

[3]Department of Pathology, University of California, San Francisco

[4]Department of Urology, University of California, San Francisco

[5]Graduate Group in Bioengineering, University of California, San Francisco and Berkeley

Abstract

Purpose—To evaluate a semi-automatic software-based method of registering in vivo prostate magnetic resonance (MR) images to digital histopathology images using two approaches: 1) in which the prostates were molded to simulate distortion due to the endorectal imaging coil prior to fixation, and 2) in which the prostates were not molded.

Materials and Methods—T2-weighted MR images and digitized whole-mount histopathology images were acquired for twenty-six patients with biopsy-confirmed prostate cancer who underwent radical prostatectomy. Ten excised prostates were molded prior to fixation. A semi-automatic method was used to align MR images to histopathology. Percent overlap between MR and histopathology images, as well as distances between corresponding anatomical landmarks were calculated and used to evaluate the registration technique for molded and unmolded cases.

Results—The software successfully morphed histology-based prostate images into corresponding MR images. Percent overlap improved from 80.4±5.8% prior to morphing to 99.7±0.62% post morphing. Molded prostates had a smaller distance between landmarks (1.91±0.75mm) versus unmolded (2.34±0.68mm), $p<0.08$.

Conclusion—Molding a prostate prior to fixation provided a better alignment of internal structures within the prostate, but this did not reach statistical significance. Software-based morphing allowed for nearly complete overlap between the pathology slides and the MR images.

Keywords

prostate cancer; MRI; histopathology; registration

INTRODUCTION

It is estimated that 1 in 6 men in the United States will be diagnosed with prostate cancer during his lifetime (1). Early and accurate prostate cancer diagnosis is important in managing the disease. With the introduction of prostate-specific antigen (PSA) screening

Corresponding author: Susan M. Noworolski, PhD, Department of Radiology and Biomedical Imaging, UCSF, 185 Berry Street, Suite 350, San Francisco, CA, 94107, Phone: 415-353-9409, Fax: 415-353-9423, Susan.Noworolski@ucsf.edu.

early diagnosis and treatment of prostate cancer became possible (2). While radical, whole-gland therapy is favored for treatment of advanced, often multifocal prostate cancer, such an approach is associated with a host of long-term genitourinary and rectal side effects (3). A targeted treatment might be preferred for patients presenting with less advanced disease. Focal treatments however require accurate disease localization, staging, and monitoring (4–5). MRI imaging is a noninvasive technique that can be used in detection and localization of prostate cancer (6–7). MRI is poised to play a significant role in the image-guided targeted biopsies and the planning of targeted treatments such as high intensity focused ultrasound (HIFU), radiofrequency ablation (RFA), cryosurgery, photodynamic therapy (PDT) or brachytherapy (8).

To establish the validity of imaging findings, accurate mapping between in-vivo MRI and digitized pathology images of the resected prostate is essential. Currently there is no established technique that allows for an accurate and timely alignment of postoperative histology images to preoperative in-vivo MR images obtained with an endorectal coil. Although the endorectal coil introduces prostate deformation, it offers a significant improvement in signal to noise ratio and spatial resolution (9).

Several factors hinder registration efforts including prostate distortion during scanning, particularly due to an endorectal coil (10), specimen shrinkage during formalin fixation on the order of 10–15% (11–12), prostate deformation during surgery, and differences in slicing plane angles (13). Additional factors such as the time between the MR scan and the surgery may further impede registration.

Registration methods based on anatomical landmarks (14), fiducial markers (15), biomechanical modeling (16), multiattribute combined mutual information (17), and spatially weighted mutual information (18) have been described in the literature. These can require subjective and time consuming user-intervention (14,19–20), make assumptions about the tissue distortion (17,21–22), or require additional information, such as MR imaging of the ex vivo prostate gland (14,19) or placement of fiducial markers (15,20). The purpose of this study was to evaluate a semi-automatic software-based method of registering digital histopathology images to in vivo prostate magnetic resonance (MR) images using two approaches. These groups were: 1) in which the prostates were molded prior to fixation to replicate the mechanical distortion due to the endorectal coil, and 2) in which the prostates were not molded.

MATERIALS AND METHODS

Patients

This study was approved by the Committee on Human Research at this institution and was compliant with the Health Insurance Portability and Accountability Act. Written, informed consent was obtained from all subjects. Twenty-six patients who underwent radical prostatectomy for a biopsy-proven prostate cancer were studied. Patients who underwent treatment for their prostate cancer prior to surgery or whose surgery was more than 120 days after their MRI were excluded from the study. The patients' mean age was 62.7 ± 5.8 years and the average Gleason score was 7.2, range GS 6 to GS 9. For this study, the time interval between MRI scan and prostatectomy was 23.4 days, ranging from 2 to 97 days. Patient characteristics are summarized in Table 1.

MR Imaging

All patients were imaged with an expandable balloon endorectal coil (Medrad, Inc., Indianola, PA, USA) and the GE pelvic phased array on a 3T MR scanner (GE Healthcare, Waukesha, WI, USA). Fast spin echo (FSE) T2-weighted images were acquired in an

oblique axial plane with FOV = 18 cm, slice thickness = 3mm, matrix = 256 × 256, and TR/TE = 6000/96. Images were corrected for the inhomogeneous reception profile associated with the combined endorectal coil and pelvic phased array (23).

Molding

After surgery, prostates were weighed and inked. Ten patients had their prostates molded. Molding was accomplished by securing the excised prostate within a plastic mesh basket prior to fixation (Figure 1). This basket was made in-house of heat sensitive moldable plastic and was designed such that the posterior side of the prostate underwent a concave curvature, intended to imitate the inflated endorectal probe. A cover was secured to the anterior portion of the prostate and compressed with rubber bands in the anterior/posterior direction, approximately by 15%, the compression typically observed with an endorectal probe (10). Prostate dimensions noted on T2-weighted MRI images were provided as a reference for molding. An opening was made in the basket to accommodate the seminal vesicles and vas deferentia.

All molded and unmolded prostatectomy specimens were formalin-fixed for at least 24 hours. Prostates were then serially cross-sectioned from apex to base at 3–4mm intervals using a manual meat slicer (Hobart, Troy, OH, USA). Tissue slices were embedded in paraffin, cut as whole-mount histologic sections and stained with hematoxylin and eosin. Slides were arranged from superior to inferior in two columns in an 8.5 × 11 inch space and digitized as a single image per sheet. Ten minutes per prostate were required to complete digitization.

Registration

In-house software written in C and Image Magick (ImageMagick Studio LLC, Landenberg, PA, USA) were used to manipulate the images. The digitized histopathology images were automatically cropped into slices (Figure 2a). Label sides were automatically detected based upon more than 5 blue or green pixels found on the right-most or left-most 200 pixels within the image. Extraneous markings were removed automatically by identifying non-violet pixels and surrounding pixels. Images were visually inspected and any remaining markings removed (Figure 2b). Pathology images were visually matched to corresponding axial T2w images according to their level in the prostate and common anatomical landmarks. Prostates were manually segmented from surrounding tissues on T2w images (Figure 2c). Manual steps of matching pathology to the MR images and segmenting the prostate on the MR images required 25 minutes per prostate to complete. Pathology slides were automatically centered and rotated to align with the corresponding MR images (Figure 2b). Next, pathology images were globally stretched or shrunk to correspond to the T2w images (global alignment). In the second stage, pathology images were stretched or shrunk differently in the right-left direction and in the anterior-posterior direction to match the maximum extent in each direction to that of the T2w images (x-y alignment). In the final stage, each row and each column in a pathology image was stretched or shrunk to match the MRI prostate, first in the left-to-right direction and then in the anterior-to-posterior direction (line-by-line alignment) (Figure 2d). Automatic image processing steps required less than a minute to complete.

Registration Assessment

The accuracy of registration was assessed in two ways. First, the percent overlap between pathology and MR images was calculated and compared for each alignment stage. Second, three visually identified landmarks marking the boundary of the peripheral zone and the central gland were placed at approximately midline, then midway between the midline and the left side, and lastly, midway between the midline and the right side on a midgland level

in each set of images. Distances between these landmarks in-plane were compared on an aligned midgland pathology slide and on the corresponding MR slice for all cases. Evaluations were made for Stage I – global alignment, Stage II – x-y alignment, and Stage III – line-by-line alignment for both the molded and unmolded cases. Alignment metrics were compared between the molded and unmolded cases. Using the right and the left-side landmark coordinates in-plane rotation angles for landmarks placed on the pathology images and the MR images were computed for molded and unmolded prostates at both x-y and line-by-line alignment stages.

Factors Potentially Impacting Alignment

Gleason Score obtained during surgery, gland volume as measured by visually outlining the gland on the T2-weighted images, gland weight as measured post-surgery, age and serum prostate specific antigen (PSA) within a year of surgery were measured or obtained. The alignment metrics of this study were compared with each of these metrics: Gleason Score, gland volume, gland weight, age, and PSA.

Statistical Methods

Statistical analyses were carried out using JMP software (JMP, Version 10, SAS Institute Inc., Cary, NC). Distances between anatomical landmarks for molded and unmolded prostates were computed. The mean and standard deviation were calculated for the two groups and a Student t-test was performed. The percent overlap mean and standard deviation values were calculated for each stage of the morphing process for molded and unmolded prostates. A Wilcoxon signed rank test of matched pairs for pair-wise comparison of mean values within a patient for percent overlap at each stage in the alignment process was done. For comparisons of patient characteristics between molded and unmolded, t-tests were done if the distributions were normal, and a Wilcoxon test used if not normally distributed. A p-value of 0.05 was used to define significance.

RESULTS

Patient demographics are given in Table 1, demonstrating no significant difference between molded and unmolded groups in terms of age and Gleason Score ($p>0.1$, t-tests), or in terms of prostate volume, prostate weight, days to surgery, or tumor volume ($p>0.1$, Wilcoxon test). PSA was variable, with a maximum value of 38.5 ng/mL in the unmolded group compared to 8.5 ng/mL in the molded group, and was significantly higher in the unmolded cases, $p<0.05$, Wilcoxon test. Without this outlier of 38.5 ng/mL which was more than two times higher than any other value in the group, the PSA was not significantly different between the groups.

An example of images from a patient with a biopsy-proven cancer (Gleason 3+3) and a PSA level of 5.5 ng/mL, who underwent prostatectomy, is shown in Figure 3. This excised prostate was molded prior to fixation. Figure 3 demonstrates that the compression and induced curvature experienced by the gland in the anterior-posterior direction due to the basket allowed the prostate to better resemble the shape of its MR counterpart, yielding a global alignment %overlap of 85.5%. In Figure 4 are images from a patient with a biopsy-proven cancer (Gleason 3+4) and a PSA level of 6.2 ng/mL, who underwent prostatectomy. This excised prostate was not molded. Figure 4 illustrates that the prostate compression and induced curvature due to the endorectal probe seen on the MR image is not observed on the corresponding histology slice for the unmolded prostate. This case had a %overlap at the global alignment stage of 72.2%, which was less than the molded case of Figure 3.

Analyses

When percent overlap between MR images and histopathology was calculated for global, x-y, and line-by-line alignment stages, there were no statistically significant differences between percent overlap values for molded and unmolded groups. With global alignment, molded prostates had 79.1±5.6% and unmolded prostates had 81.6±5.9% overlap with MR images, $p>0.3$. The percent overlap increased to 84.9±5.4% and 84.4±6.3% for x-y aligned molded and unmolded prostates respectively, $p>0.97$. In the final stage of line-by-line alignment, percent overlap reached 99.7±0.46% for molded and 99.7±0.71% for unmolded prostates, $p>0.97$. In a pair-wise comparison, it was determined that on average, percent overlap increased by 3.95% between global and x-y alignment stages, and then by another 15.1% between x-y and line-by-line alignment stages, $p<0.001$.

An example shown in Figure 5 demonstrates the three landmarks positioned within the prostate on the MR slice (Figure 5a), as well as the corresponding x-y (Figure 5b) and line-by-line (Figure 5c) aligned histopathology images. For each landmark, the in-plane distances between MR and the x-y aligned pathology coordinates were calculated. The mean distance for the three landmarks was determined to be 1.47mm for this case. Also, for each landmark, the distance between the MR and the line-by-line aligned pathology image was computed; the mean distance for the three landmarks was determined to be 1.13mm. Landmark distances were calculated for midgland slices for all molded and unmolded prostates. For both groups, the landmark distance values were normally distributed. For x-y aligned prostates, the average distance between corresponding landmarks was 2.34±0.68mm for unmolded and 1.91±0.75mm for molded prostates (Table 2). There was a trend toward molded prostates having smaller average and maximum landmark distances, but with a p-value of 0.079, the result did not reach significance. For the line-by-line alignment stage, the average distance between corresponding landmarks was 1.67±0.58mm for unmolded and 1.62±0.58mm for molded prostates. With a p-value of 0.422, there were no statistically significant differences between the two groups. There were no differences in the time it took to process the specimens in each group. For every prostate, approximately 45 minutes were required to complete all the alignment steps.

There was no significant in-plane rotation between the pathology and the MR images, based on the right and left side landmark coordinates. For the x-y alignment stage, the mean rotation angle was −0.58 ±3.1 degrees for unmolded and −1.04±1.30 degrees for molded prostates. With a p-value of 0.48, there were no statistically significant differences between the two groups. For the line-by-line alignment, the mean rotation angle was −0.66±4.21 degrees for unmolded and −0.59±1.87 degrees for molded prostates. Once again, with a p-value of 0.38, no statistically significant differences between the molded and the unmolded prostates

No trends for percent overlap or landmark distances were observed to be associated with Gleason Score, tumor volume, prostate weight, PSA, or prostate volume, $p>0.05$ for all comparisons, linear regression. Landmark distances before and after line-by-line alignment significantly increased with age, $p<0.05$, linear regression.

DISCUSSION

This study demonstrated that computationally morphing the prostate allowed an almost complete overlap of 99.7% between the pathology slides and the MR images with good alignment of internal structures. These results were robust across different prostates, with no bias in alignment when compared to Gleason Score, tumor volume, prostate weight, PSA or prostate volume. The internal alignment was worse for older patients although no statistical corrections were made for the multiple comparisons performed. After the global alignment

and the separate x-y stretching/compressing, the average distance between landmarks was 2.17±0.73 mm, ranging from 0.87mm to 3.54mm. After the final line-by-line alignment stage, this distance decreased to an average of 1.65±0.57mm, ranging from 0.693mm to 3.27mm. These internal distances between structures were less than the typical distortion caused by the endorectal coil, which are an average anterior-posterior compression of 4.1 mm and an average right-left expansion of 3.7 mm (10). This demonstrates that the alignment at least partially compensates for the endorectal coil distortion. Therefore, this technique can be used to align the histopathology to other functional imaging modalities obtained with an endorectal coil such as MR spectroscopy, diffusion-weighted imaging, and the dynamic contrast enhanced MR imaging.

The first part of our registration method entailed a rigid alignment with global stretching/ shrinking separately in the×and y directions. We obtained an internal alignment of 2.34±0.68 mm for unmolded prostates, which was similar to other studies in the literature, which report registration errors ranging from 2.3 to 2.89 mm (14–16). These studies involved user intervention to identify internal landmarks (14), additional scanning of the ex vivo prostate, ex-vivo imaging (14,19) and/or fiducial markers (15,20) to guide the histopathology sectioning of the gland. In contrast, our method did not require extensive user intervention or ex vivo prostate scans, which may be difficult to incorporate into a standard clinical protocol. Furthermore, in a clinical setting time efficiency is crucial. Our computational method required less than an hour to align histopathology images for an entire prostate to the corresponding in-vivo MR images, while other groups reported registration times ranging from several hours to several days (14–16).

The second stage of our alignment incorporated non-rigid registration and resulted in internal alignment to landmarks of 1.67±0.58mm for unmolded prostates, without significant rotation between histopathology and the MR images. These results are similar or better than other automatic alignment methods reported in the literature. Patel et al based an alignment on spatially weighted mutual information, which had virtually the same performance as our method, with 1.65 mm registration error, ranging from 1.05 mm to 2.03 mm (18). An advantage of their method is that it does not necessitate prostate segmentation from MRI images; however, the results presented in the study were limited to 7 slices collected from 2 patients and require further exploration in a larger cohort. Samavati et al described a biomechanical model-based deformable registration approach and reported a target registration error of 2.1mm for a finite element modeling registration method (16). For this method, several ex-vivo scans were done and additional magnetic resonance elastography (MRE) studies had to be carried out on the excised prostate specimens. The sample size in this study was limited to 4 prostates. Other non-rigid methods that used additional information performed slightly better. A method based on user-identified landmarks within both the in vivo and ex vivo prostate resulted in a 1.59 mm registration error (14). However, with the sample size of 3, these findings need to be verified with a larger sample size. The method by Ward et al., which based histology specimen slicing on ex vivo MRI with fiducial markers, attained a 1.1 mm error in a study of 13 prostate specimens (15). While our method had a slightly higher registration error, it was similar and did not require scans of the ex vivo gland or time consuming and subjective identification of landmarks within the gland and was evaluated on more, specifically 26, subjects. Overall, compared to others in the literature, our alignment methods produced similar or better results, required less time, and were validated in a larger cohort of patients.

This study also looked at the effects of molding on registration outcomes. Molding the prostate during pathological preparation of the gland provided a better alignment of internal structures within the prostate, but this did not reach significance. Most prostate molding efforts described in the literature involve post formalin fixation molding done with patient-

specific molds, which can be expensive and time-consuming to make (24–26). Formalin fixation makes the gland rigid and tough, limiting the extent to which the prostate can be molded. To avoid this, prostates in this study were fixed while in the molding basket. We saw a trend toward molded prostates having a better alignment of internal structures, which did not reach statistical significance. While molding tended to aid the alignment of internal structures at the x-y alignment stage, the line-by-line alignment seemed to compensate for this, resulting in a similar internal alignment of the molded and unmolded prostates, implying that molding is not required if the line-by-line alignment is performed. The trend in improvement in the alignment of internal structures post x-y alignment for molded cases versus unmolded cases suggests that further improvements in our molding technique may result in further improvement in alignment.

There were a few limitations to this study. First, we had a single size basket that was used to mold prostates that ranged in size from 15.2ml to 75.8ml. Individualized or tailored sized baskets may have improved the alignment. Second, the compression of the gland varied across subjects. While efforts were made to defer to MR images for guidance, properly modulating compression remains difficult. Third, the alignment of the histopathology slides to the corresponding MR images was done in 2D, which assumes that the prostate specimen was sliced along the same plane as the in vivo MR images were acquired. While the MR images were acquired in an anatomic, axial plane, this may not necessarily match the orientation of the prostate ex vivo, leading to sections obtained at different angles than the MRI. Fourth, we used a manual meat slicer to standardize the slicing of the histopathology sections; if any cases or portions of prostates varied in their shrinkage with fixation, the histology slices may not correspond to the MR images. Fifth, histopathology slices represent microns of tissue whereas the MR images span 3 mm of tissue and may not correspond well. Sixth, while our method tried to incorporate mechanical compression to mimic the in vivo prostate deformation and then non-rigid registration, distortion within the gland may have been more pronounced. This could occur when a BPH nodule shifts or expands out of plane or tears the tissue during processing. Other limitations include: 1) the use of subjective, user-identification of the prostate within the MR images and user confirmation or modification of the identification of the prostate within the histopathology images; 2) the use of subjective, user-identified landmarks within the gland to assess the alignment, which may affect the registration metrics. However these landmarks were not used during the alignment procedure, which was automated; and 3) a limited number of cases were studied, which may have hindered detection of significant differences between the molded and unmolded prostate alignments.

In conclusion, this study presented a semi-automatic alignment method demonstrating an almost complete overlap between histopathology slides and MR images with good alignment of internal structures. While user-intervention was required to segment the prostate in the MR images and to assess and adjust the automatic segmentation, if necessary, on the histopathology, neither user-intervention nor additional scans were required during the alignment procedures. Thus, this is a promising technique for more broad use for alignment of histopathology to MR images. Molding the prostate during pathological preparation of the gland may provide a better alignment of internal structures within the prostate, but this did not reach significance.

Acknowledgments

Grant Support: NIH: RO1 CA148708, ACS: MRSG-0508701, NIH R01 CA137207

REFERENCES

1. American Cancer Society. Cancer Facts and Figures 2012. Atlanta: American Cancer Society; 2012.
2. Grossfeld GD, Carroll PR. Prostate cancer early detection: a clinical perspective. Epidemiol Rev. 2001; 23(1):173–180. [PubMed: 11588845]
3. Sanda MG, Dunn RL, Michalski J, et al. Quality of life and satisfaction with outcome among prostate-cancer survivors. N Engl J Med. 2008; 358(12):1250–1261. [PubMed: 18354103]
4. Turkbey B, Pinto PA, Choyke PL. Imaging techniques for prostate cancer: implications for focal therapy. Nat Rev Urol. 2009; 6(4):191–203. [PubMed: 19352394]
5. Makarov DV, Partin AW. Focal therapy for prostate cancer. Rev Urol. 2008; 10(1):81–82. [PubMed: 18470280]
6. Fuchsjager M, Akin O, Shukla-Dave A, Pucar D, Hricak H. The role of MRI and MRSI in diagnosis, treatment selection, and post-treatment follow-up for prostate cancer. Clin Adv Hematol Oncol. 2009; 7(3):193–202. [PubMed: 19398944]
7. Kurhanewicz J, Vigneron D, Carroll P, Coakley F. Multiparametric magnetic resonance imaging in prostate cancer: present and future. Curr Opin Urol. 2008; 18(1):71–77. [PubMed: 18090494]
8. Bomers JG, Sedelaar JP, Barentsz JO, Futterer JJ. MRI-guided interventions for the treatment of prostate cancer. AJR Am J Roentgenol. 2012; 199(4):714–720. [PubMed: 22997360]
9. Hricak H, White S, Vigneron D, et al. Carcinoma of the prostate gland: MR imaging with pelvic phased-array coils versus integrated endorectal--pelvic phased-array coils. Radiology. 1994; 193(3): 703–709. [PubMed: 7972810]
10. Kim Y, Hsu IC, Pouliot J, Noworolski SM, Vigneron DB, Kurhanewicz J. Expandable and rigid endorectal coils for prostate MRI: impact on prostate distortion and rigid image registration. Med Phys. 2005; 32(12):3569–3578. [PubMed: 16475755]
11. Jonmarker S, Valdman A, Lindberg A, Hellstrom M, Egevad L. Tissue shrinkage after fixation with formalin injection of prostatectomy specimens. Virchows Arch. 2006; 449(3):297–301. [PubMed: 16909262]
12. Schned AR, Wheeler KJ, Hodorowski CA, et al. Tissue-shrinkage correction factor in the calculation of prostate cancer volume. Am J Surg Pathol. 1996; 20(12):1501–1506. [PubMed: 8944043]
13. Jager GJ, Ruijter ET, van de Kaa CA, et al. Local staging of prostate cancer with endorectal MR imaging: correlation with histopathology. AJR Am J Roentgenol. 1996; 166(4):845–852. [PubMed: 8610561]
14. Orczyk C, Mikheev A, Rosenkrantz A, Melamed J, Taneja SS, Rusinek H. Imaging of prostate cancer: a platform for 3D co-registration of in-vivo MRI ex-vivo MRI and pathology. 2012:83162M–83162M.
15. Ward AD, Crukley C, McKenzie CA, et al. Prostate: Registration of Digital Histopathologic Images to in Vivo MR Images Acquired by Using Endorectal Receive Coil. Radiology. 2012; 263(3):856–864. [PubMed: 22474671]
16. Samavati N, McGrath DM, Lee J, et al. Biomechanical model-based deformable registration of MRI and histopathology for clinical prostatectomy. J Pathol Inform. 2011; 2:S10. [PubMed: 22811954]
17. Chappelow J, Bloch BN, Rofsky N, et al. Elastic registration of multimodal prostate MRI and histology via multiattribute combined mutual information. Med Phys. 2011; 38(4):2005–2018. [PubMed: 21626933]
18. Patel P, Chappelow J, Tomaszewski J, et al. Spatially weighted mutual information (SWMI) for registration of digitally reconstructed ex vivo whole mount histology and in vivo prostate MRI. Conf Proc IEEE Eng Med Biol Soc. 2011; 2011:6269–6272. [PubMed: 22255771]
19. Park H, Piert MR, Khan A, et al. Registration methodology for histological sections and in vivo imaging of human prostate. Acad Radiol. 2008; 15(8):1027–1039. [PubMed: 18620123]
20. Kimm SY, Tarin TV, Lee JH, et al. Methods for registration of magnetic resonance images of ex vivo prostate specimens with histology. J Magn Reson Imaging. 2012; 36(1):206–212. [PubMed: 22359365]

21. Mazaheri Y, Bokacheva L, Kroon DJ, et al. Semi-automatic deformable registration of prostate MR images to pathological slices. J Magn Reson Imaging. 2010; 32(5):1149–1157. [PubMed: 21031521]

22. Cheung MR, Krishnan K. Using manual prostate contours to enhance deformable registration of endorectal MRI. Comput Methods Programs Biomed. 2012

23. Noworolski SM, Reed GD, Kurhanewicz J, Vigneron DB. Post-Processing Correction of the Endorectal Coil Reception Effects in MR Spectroscopic Imaging of the Prostate. Journal of Magnetic Resonance Imaging. 2010; 32(3):654–662. [PubMed: 20815064]

24. Shah V, Pohida T, Turkbey B, et al. A method for correlating in vivo prostate magnetic resonance imaging and histopathology using individualized magnetic resonance-based molds. Rev Sci Instrum. 2009; 80(10):104301. [PubMed: 19895076]

25. Turkbey B, Pinto PA, Mani H, et al. Prostate cancer: value of multiparametric MR imaging at 3 T for detection--histopathologic correlation. Radiology. 2010; 255(1):89–99. [PubMed: 20308447]

26. Trivedi H, Turkbey B, Rastinehad AR, et al. Use of patient-specific MRI-based prostate mold for validation of multiparametric MRI in localization of prostate cancer. Urology. 2012; 79(1):233–239. [PubMed: 22202553]

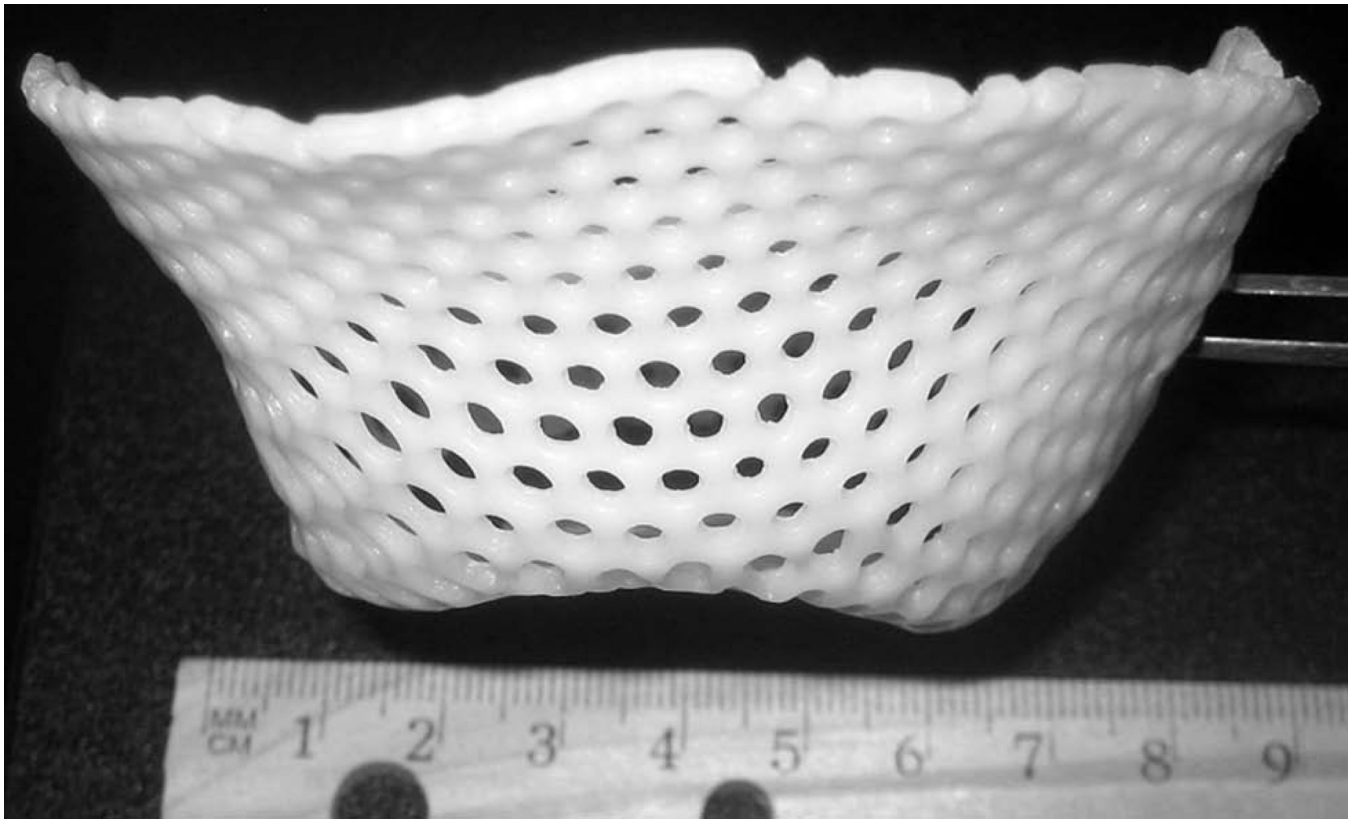

Figure 1.
The mesh basket used for molding the excised prostates.

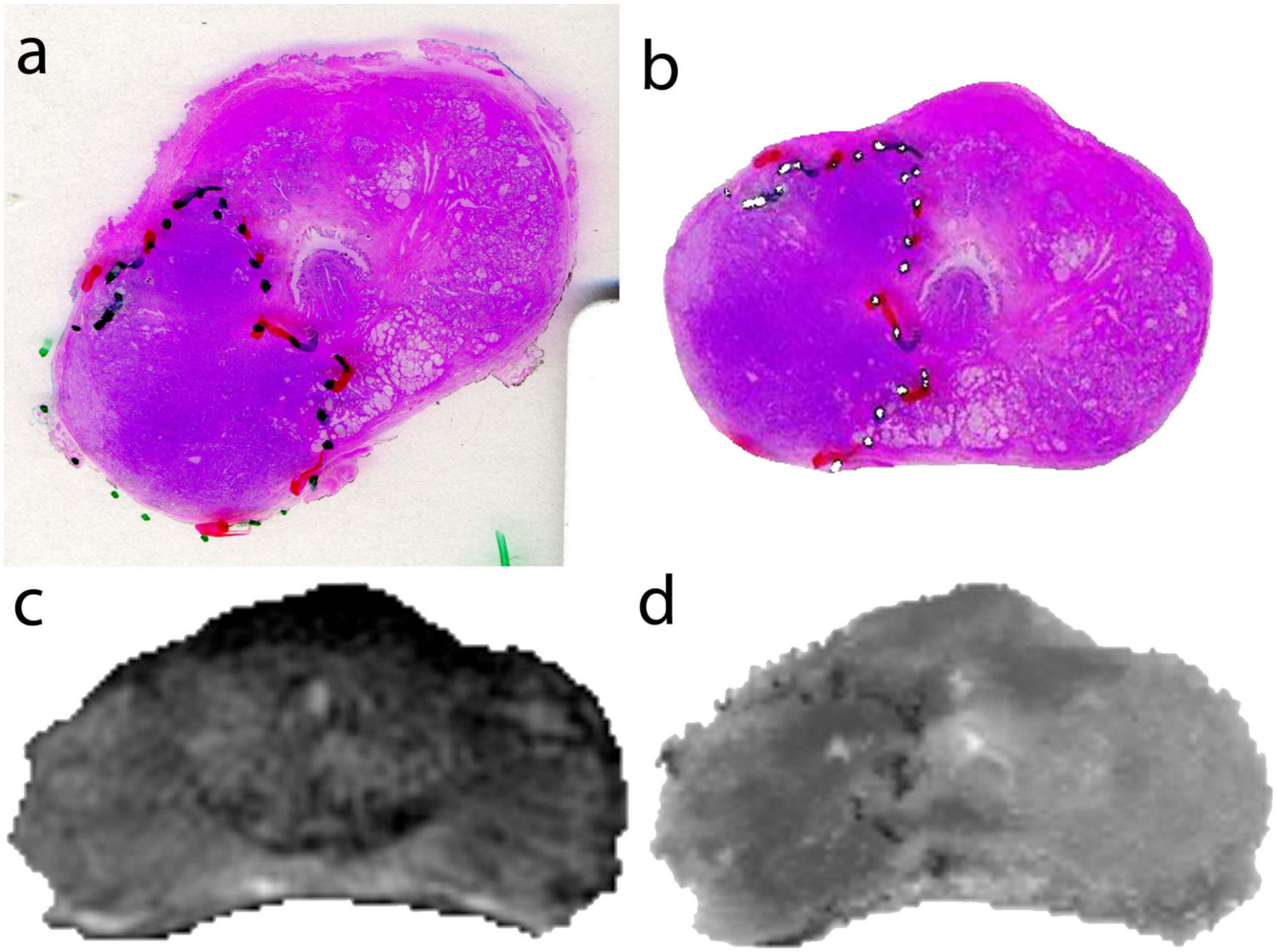

Figure 2.
Alignment steps: a. Original histopathology slide. b. Slide from (a) with background markings removed. c. Aligned histopathology slide from (b). d. T2-weighted MR image.

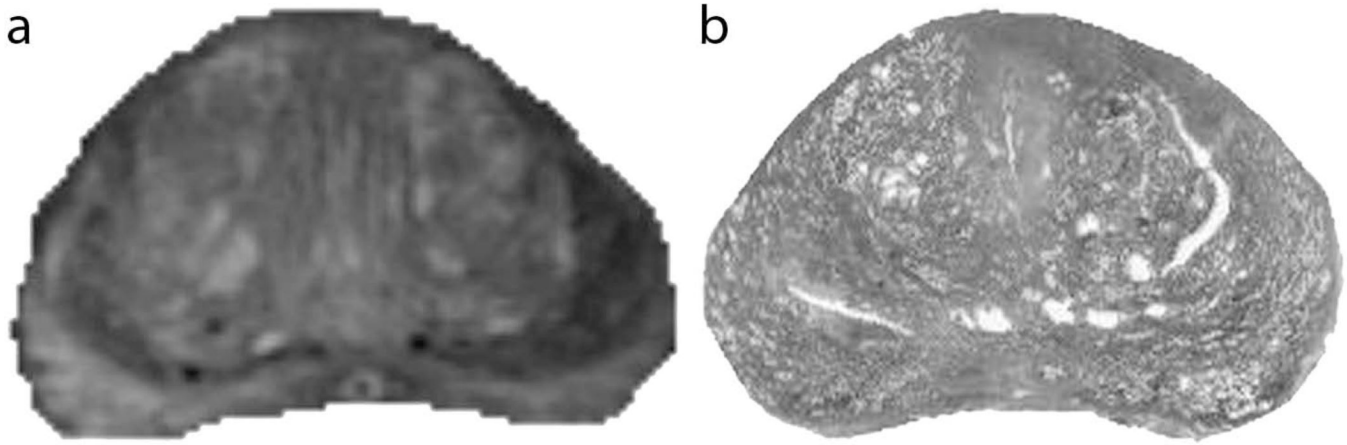

Figure 3.
Molded prostate: a. Axial T2-weighted MR image. b. Corresponding histopathology slide.

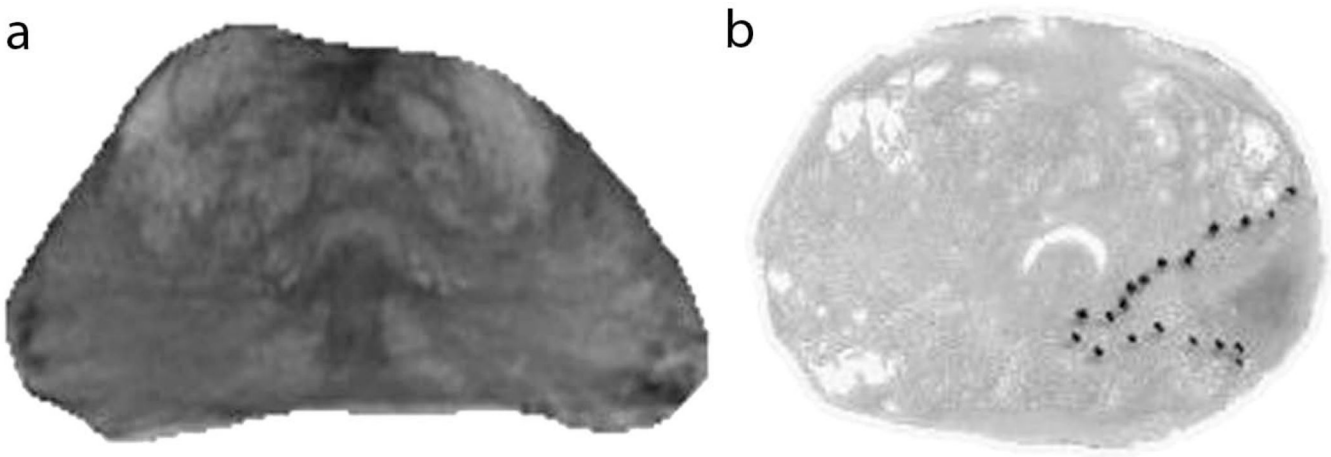

Figure 4.
Unmolded prostate: a. Axial T2-weighted MR image. b. Corresponding histopathology slide.

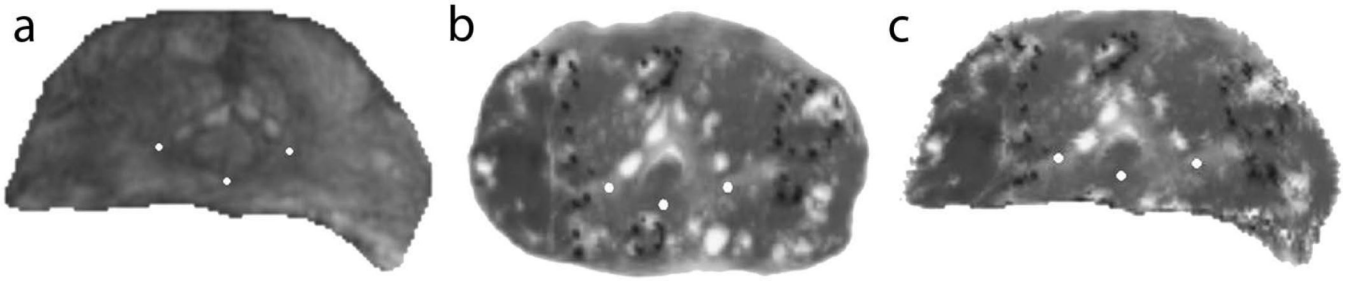

Figure 5.
Landmarks shown on a. Axial T2-weighted MR image. b. Corresponding histopathology slide. c. Aligned histopathology slide from (b).

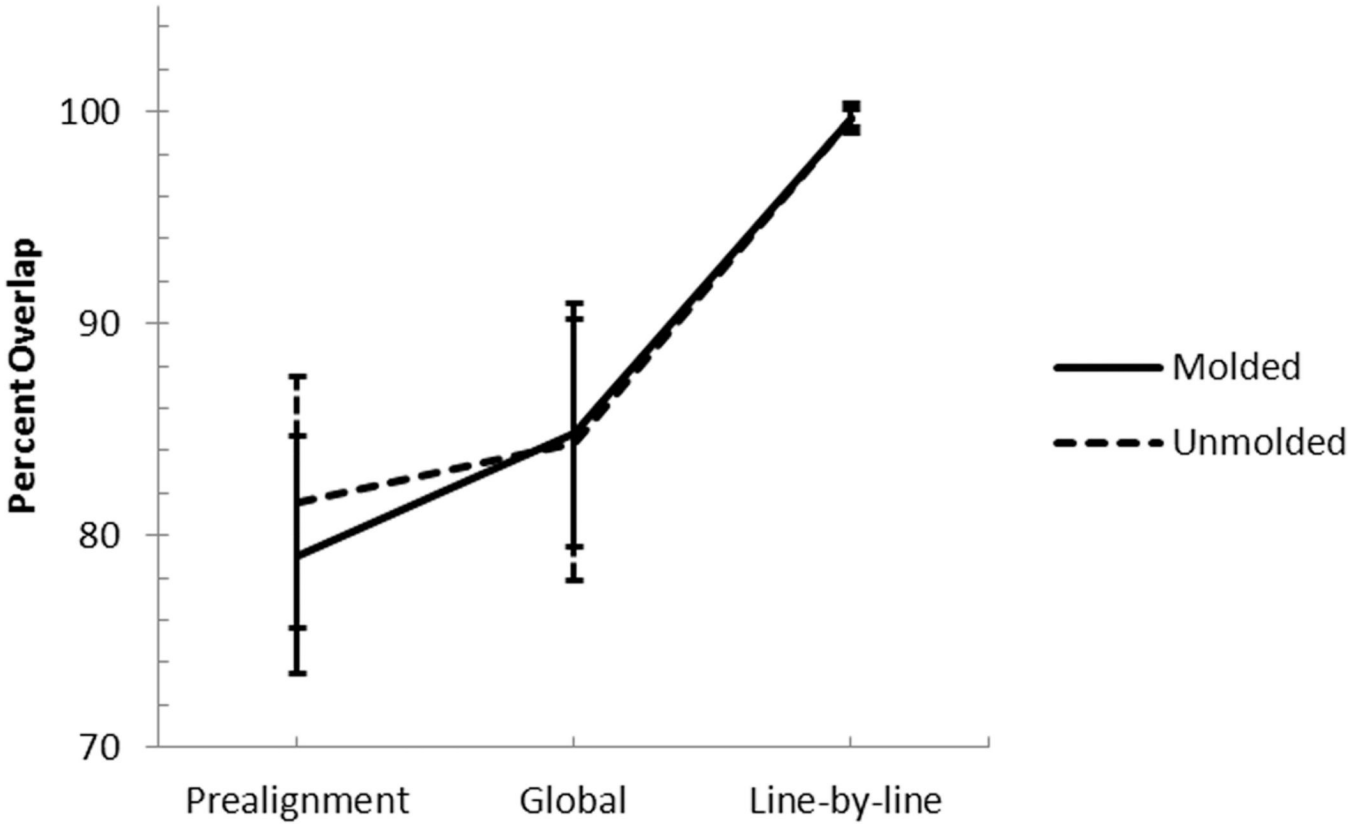

Figure 6.
Percent overlap between histopathology and MR images at the different stages of alignment. Error bars indicate standard deviation.

Table 1

Patient Characteristics

Variable	Molded (N=10)	Unmolded (N=16)
Age (years)	60.4 (6.0)	64.1 (5.3)
Prostate weight (gm)	49.6 (21.4)	43.8 (9.7)
Prostate volume (cm^3)	36.0 (19.0)	29.7 (9.6)
Gleason score	7.0 (1.0)	7.4 (0.9)
Days to surgery	20.5 (14.3)	25.2 (28.9)
PSA (ng/mL)	4.3 (2.1)	8.7 (8.4)
Tumor volume (cm^3)	2.8 (2.9)	5.1 (5.4)

Mean (SD)

Table 2

Three Point Landmark Distance

Alignment	Molded	Unmolded
Global		
Mean (SD)	1.91 (0.75)	2.34 (0.68)
Min, Max (mm)	0.870, 3.08	1.13, 3.54
Line-by-line		
Mean (SD)	1.62 (0.58)	1.67 (0.58)
Min, Max (mm)	0.955, 2.80	0.693, 3.27